


Glued-in-rod timber joints: analytical model and finite element simulation

A. Hassanieh  · H. R. Valipour · M. A. Bradford · R. Jockwer

Received: 8 January 2018 / Accepted: 26 April 2018
© RILEM 2018

Abstract In this paper, a closed form analytical solution for glued-in-rod (GiR) joints is derived by solving the governing differential equations and accurately applying the boundary conditions in a cylindrical coordinate system for a GiR joint comprising of a rod, adhesive (glue) and timber. The results of the analytical model are compared with 3D continuum finite element simulations and it is shown that the closed-form solution developed can estimate the stress distribution in the adhesive and adherents (rod and timber) with good accuracy. Furthermore, the stiffness of GiR timber joints can be obtained from this analytical model. Closed-form solutions for pull–pull and pull–push test setup configurations are compared and it is shown that the maximum shear stress in the adhesive-adherent interface in a pull–push configuration is around 20% higher than that of the pull–pull counterpart. The typically (around 20%) lower strength of GiR joints in pull–push experiments compared to that of pull–pull tests can be attributed to this higher maximum shear stress which is predicted

by the analytical model. A parametric study is carried out using the FE and analytical models and the effects of different variables on the distribution of stresses in the adhesive and adherents are studied.

Keywords Adhesive · Glued-in-rod · Joints · Pull–pull · Pull–push · Timber

1 Introduction

Adhesively-bonded tubular joints are among the most common types of connections used in civil and mechanical engineering applications. Steel rods that are anchored in concrete or rock are simple examples of tubular joints that have been used for many decades in civil construction [1]. Glued-in-rod (GiR) timber connections are another example of adhesively-bonded joints that are gaining popularity in large-scale timber construction [2]. In addition to timber–timber connections, GiR joints can efficiently facilitate the connection between timber elements and other structural elements made of concrete and/or steel.

GiR joints have been used in axially-loaded connections, in moment-resisting beam-to-column connections [3] and in column-to-foundation connections for timber structures [4–6]. Moreover, GiR connections have been used for the reinforcing and strengthening of old and new timber elements, particularly

A. Hassanieh (✉) · H. R. Valipour · M. A. Bradford
School of Civil and Environmental Engineering, Centre
for Infrastructure Engineering and Safety, UNSW
Australia, UNSW Sydney, Sydney, NSW 2052, Australia
e-mail: a.hassanieh@unsw.edu.au

R. Jockwer
Department of Civil, Environmental and Geomatic
Engineering, Institute of Structural Engineering, ETH
Zürich, 8093 Zurich, Switzerland

those made from softwood. Additionally, the application of GiRs for reinforcing and strengthening timber in tension loaded perpendicular to the grain (notched beams, beams with holes), improving the shear strength (preventing early shear failure) of timber, preventing timber crushing due to excessive compression perpendicular to the grain at the supports (or the location of concentrated loads) and improving the bending strength of timber beams has been investigated [6].

Extensive experimental tests have been conducted on GiR timber joints as part of the GIROD project that aimed to create a database for evaluating the effects of different variables (viz. the joint geometry and material properties, adhesive type and loading direction with respect to the timber grain) on the behaviour of GiR timber joints [7]. Two comprehensive experimental studies on GiR joints in glulam made of Spruce lamella loaded parallel to the grain and perpendicular to the grain were conducted by Steiger et al. [8] and Widmann et al. [9]. The influence of the wood density and the geometry of the joints on the load carrying capacity of the GiR timber joints were considered, and empirical models for estimating the pull-out capacity of the GiR joints with respect to the wood density and the length to diameter ratio of the rods were proposed [8, 9]. Laboratory experiments have also been conducted on GiR joints made from hardwoods [10] and a comparison between the failure modes of GiR hardwood and softwood (Spruce) joints has been reported [11]. While steel rods are typically used in GiR timber joints, Madhoushi et al. [12] performed static and cyclic fatigue tests on GiR joints with glass fibre reinforced polymer rods.

In addition to laboratory experiments, the behaviour of GiR timber joints has been studied numerically and analytically [12–15]. A full 3D finite element (FE) analysis of GiR specimens in pull–pull tests was carried out by Serrano [12] and Madhousgi and by Ansell [13]. Furthermore, axisymmetric FE models of the joints under axial load have been developed by Del Senno et al. [14] and a FE analysis of GiR beam-to-beam timber joints was performed by Xu et al. [15]. Despite the versatility of FE models as a powerful tool for capturing the behaviour of structural connections, analyses of GiR timber joints using conventional FE models is computationally demanding owing both to the anisotropy of timber and to the very small mesh size required for adequately representing the thin layer

of the adhesive and incorporating the gradient of the stresses near the boundaries. Accordingly, several studies have focused on the development of closed-form analytical solutions for adhesively bonded joints that can be used in analysis, as well as in the strength design of joints. Significant effort has been devoted to the development of analytical solutions for adhesively-bonded cylindrical joints such as glued-in-rods. One of the first closed-form solutions for an axially bonded tube was proposed by Lubkin et al. [16] some sixty years ago. Minimisation of the complementary energy was used by Shi et al. [17] to derive an approximate solution for axially-loaded tubular joints, while Nemes et al. [18] derived an analytical model assuming anisotropic behaviour for the adherents in an axisymmetric formulation, founded on a variational method using minimisation of the total potential energy. Nemes' solution was later modified by considering the radial stresses in the adherent [19]. An analytical model for the pull-out capacity of adhesively-bonded anchors was proposed by Upadhyaya et al. [20], and later a more detailed solution that accounts for the variation of the elastic modulus of the material was derived by Kumar et al. [21, 22]. More recently, solutions of weak-form models of adhesively anchored bars in concrete or rocks have been developed, with possible variations of the mechanical properties of the adhesive along the anchored length being considered [23, 24].

Accurate analyses of adhesively-bonded joints are a first step towards the safe and economic design of joints based on strength criteria. Furthermore, the stiffness of connections with GiR joints can significantly influence the performance of a structure at service loading conditions. Accordingly, this study inspired by Nemes' [18] work investigates the short-term behaviour of GiR timber joints through the development of a closed-form analytical model as well as FE simulations. In addition to distributions of stress, an analytical formulation is derived for the stiffness of GiR timber joints. The accuracy of the analytical solution in comparison with the FE models, calibrated against experimental results, is demonstrated. The calibrated FE and closed form analytical models are then employed to conduct a parametric study that elucidates the effect of different variables on the structural behaviour of the GiR timber joints.



2 Analytical model

2.1 General

The analytical models of adhesively-bonded joints are usually developed in the framework of a strength analysis [5] by incorporating prescribed stress fields into the governing differential equations of the adhesive-adherents system. Some of the assumptions adopted for stress fields in GiR joints as well the as assumptions used in this study are summarised in Table 1.

In this section, a solution is proposed for axisymmetric GiR joints in a pull–pull test setup, with the solution then being extended to a pull–push scenario by applying appropriate proper boundary conditions. The governing equations are formulated in the cylindrical coordinate system (z, r, θ) shown in Fig. 1. The inner adherent (1) and the adhesive (A) are assumed to be isotropic, but the outer adherent (2) is assumed to be transversely isotropic which can adequately represent the behaviour of timber. Following this convention, the superscripts (1), (2) and (A) denote the inner adherent, outer adherent and adhesive, respectively. The inner adherent radius is $r^{(1)} = a$, and b and c are the inner and outer radii of the outer adherent, respectively (Fig. 1). The thickness of adhesive is therefore $t^{(A)} = (b - a)$ and the thickness of the outer adherent is $t^{(2)} = (c - b)$. In addition, the following assumptions are adopted for developing the analytical solution.

- The adhesive and adherents are linear elastic with $E^{(1)}$ and $\nu^{(1)}$ being the elastic modulus and Poisson's ratio of adherent (1) (rod), $E^{(A)}$ and $\nu^{(A)}$ the elastic modulus and Poisson's ratio of the adhesive layer and $E_1^{(2)}, E_2^{(2)}, G_{12}^{(2)}, \nu_{12}^{(2)}$ the elastic

moduli, shear modulus and Poisson's ratio of adherent (2) (timber).

- The axial stresses in the adherents $\sigma_z^{(1)}$ and $\sigma_z^{(2)}$ are a function of z only, and independent of r .
- The axial stress in the adhesive is negligible, i.e. $\sigma_z^{(A)} = 0$.
- The radial σ_r and tangential σ_θ stresses are equal, i.e. $\sigma_r^{(1)} = \sigma_\theta^{(1)}, \sigma_r^{(2)} = \sigma_\theta^{(2)}, \sigma_r^{(A)} = \sigma_\theta^{(A)}$.
- The load applied to the inner adherent (rod) causes uniform normal stress $f = F/A_{\text{rod}}$ on the rod and a uniform normal stress $q = F/A_{\text{timber}}$ on cross-section of the outer adherent (timber) in the z direction on the end boundaries (Fig. 2).

The accuracy of these assumptions is demonstrated and discussed subsequently.

2.2 Equilibrium equations

In a cylindrical coordinate system, the equilibrium equations can be expressed as [19]

$$\frac{\partial \sigma_r}{\partial r} + \frac{\sigma_r - \sigma_\theta}{r} + \frac{\partial \tau_{zr}}{\partial z} = 0 \quad \rightarrow \quad \sigma_\theta = \sigma_r \quad (1)$$

$$\frac{\partial \sigma_\theta}{\partial r} = \frac{\partial \sigma_r}{\partial r} = -\frac{\partial \tau_{zr}}{\partial z}$$

and

$$\frac{\partial \tau_{zr}}{\partial r} + \frac{\tau_{zr}}{r} + \frac{\partial \sigma_z}{\partial z} = 0 \quad \rightarrow \quad \frac{\partial}{\partial r}(r\tau_{zr}) = -r \frac{\partial \sigma_z}{\partial z}. \quad (2)$$

The stress components can be obtained for the adherents using the equilibrium equations. The shear and tangential stress components in the inner adherent (rod) obtained from Eqs. (1) and (2) are

Table 1 Assumptions adopted for stress fields in different analytical models

Reference	Zone	σ_z	σ_θ	σ_r	τ_{rz}
Lubkin et al. [16]	Adhesive	—	—	$\sigma_r(z)$	$\tau_{rz}(z)$
	Adherent	$\sigma_z(z)$	—	$\sigma_r(z)$	$\tau_{rz}(z)$
Shi et al. [17]	Adhesive	—	$\sigma_\theta(r, z)$	$\sigma_r(r, z)$	$\tau_{rz}(r, z)$
	Adherent	$\sigma_z(r, z)$	$\sigma_\theta(r, z)$	$\sigma_r(z)$	$\tau_{rz}(r, z)$
Nemes et al. [18]	Adhesive	—	$\sigma_\theta(r, z)$	—	$\tau_{rz}(r, z)$
	Adherent	$\sigma_z(z)$	$\sigma_\theta(r, z)$	—	$\tau_{rz}(r, z)$
Nemes et al. [19]	Adhesive	—	$\sigma_\theta(z)$	Constant	$\tau_{rz}(r, z)$
	Adherent	$\sigma_z(z)$	$\sigma_\theta(r, z)$	$\sigma_r(r)$	$\tau_{rz}(r, z)$
This study	Adhesive	—	$\sigma_\theta(r, z)$	$\sigma_r(r, z) = \sigma_\theta$	$\tau_{rz}(r, z)$
	Adherent	$\sigma_z(z)$	$\sigma_\theta(r, z)$	$\sigma_r(r, z) = \sigma_\theta$	$\tau_{rz}(r, z)$

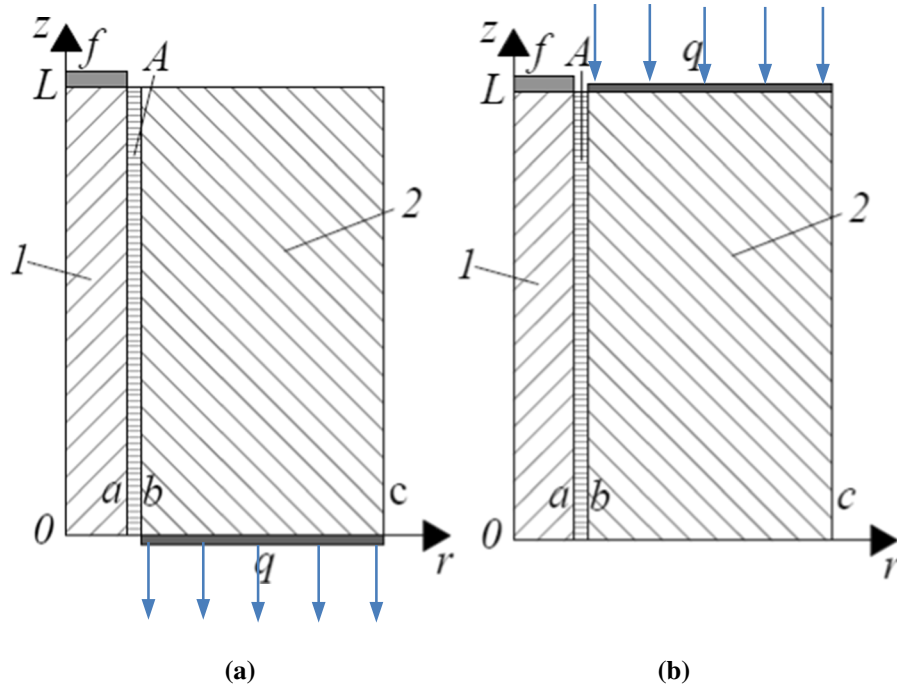


Fig. 1 Description of GiR joint and coordinate system, **a** pull–pull, **b** pull–push configuration

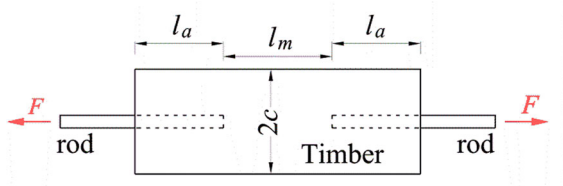


Fig. 2 Pull-pull test on glued-in-rod specimens of the GIROD project [7]

$$\tau_{rz}^{(1)} = \frac{1}{r} \int_0^r -r \left(\frac{d\sigma_z^{(1)}}{dz} \right) dr = -\frac{r}{2} \frac{d\sigma_z^{(1)}}{dz} \quad (3)$$

and

$$\sigma_\theta^{(1)} = \sigma_r^{(1)} = \int_0^r \frac{r}{2} \left(\frac{d^2\sigma_z^{(1)}}{dz^2} \right) dr = \frac{r^2}{4} \frac{d^2\sigma_z^{(1)}}{dz^2}. \quad (4)$$

Similarly, for the outer adherent (timber), the counterpart equations are

$$\tau_{rz}^{(2)} = \frac{1}{r} \int_r^c -r \left(\frac{d\sigma_z^{(2)}}{dz} \right) dr = -\left(\frac{c^2 - r^2}{2r} \right) \frac{d\sigma_z^{(2)}}{dz} \quad (5a)$$

and

$$\begin{aligned} \sigma_\theta^{(2)} = \sigma_r^{(2)} &= \int_r^c \left(\frac{c^2 - r^2}{2r} \right) \frac{d^2\sigma_z^{(2)}}{dz^2} dr \\ &= \left[\frac{1}{2} c^2 \ln\left(\frac{c}{r}\right) - \frac{1}{4} (c^2 - r^2) \right] \frac{d^2\sigma_z^{(2)}}{dz^2}. \end{aligned} \quad (6a)$$

A balance of the applied stress f and support stress q on the boundaries of the inner and outer adherents respectively, in conjunction with the assumption that $\sigma_z^{(A)} = 0$, yields (Fig. 1a)

$$a^2 \sigma_z^{(1)} + (c^2 - b^2) \sigma_z^{(2)} = a^2 f = (c^2 - b^2) q, \quad (7)$$

and rearranging Eq. (7) then produces

$$\sigma_z^{(2)} = \frac{a^2}{(c^2 - b^2)} (f - \sigma_z^{(1)}). \quad (8)$$

Substituting $\sigma_z^{(2)}$ from Eq. (8) into Eqs. (5a) and (6a) results in

$$\tau_{rz}^{(2)} = -\left(\frac{c^2 - r^2}{2r} \right) \frac{d\sigma_z^{(2)}}{dz} = \frac{a^2 (c^2 - r^2)}{2r (c^2 - b^2)} \frac{\partial \sigma_z^{(1)}}{\partial z} \quad (5b)$$

and

$$\begin{aligned}\sigma_{\theta}^{(2)} &= \sigma_r^{(2)} = \left[\frac{1}{2} c^2 \ln\left(\frac{c}{r}\right) - \frac{1}{4} (c^2 - r^2) \right] \frac{d^2 \sigma_z^{(2)}}{dz^2} \\ &= \left[\frac{1}{2} c^2 \ln\left(\frac{c}{r}\right) - \frac{1}{4} (c^2 - r^2) \right] \frac{a^2}{(c^2 - b^2)} \frac{d^2 \sigma_z^{(1)}}{dz^2}.\end{aligned}\quad (6b)$$

Further, the continuity of stresses in the adhesive layer at $r = a$ and $r = b$ leads to

$$\tau_{rz}^{(A)} = \frac{a}{2} \left[\left(\frac{r-a}{b-a} \right) \left(\frac{a}{b} + 1 \right) - 1 \right] \frac{d\sigma_z^{(1)}}{dz} \quad (9)$$

and

$$\begin{aligned}\sigma_{\theta}^{(A)} &= \sigma_r^{(A)} \\ &= \left\{ \frac{1}{2} \left[\frac{r-a}{b-a} \frac{a^2 c^2}{c^2 - b^2} \ln\left(\frac{c}{b}\right) - \frac{a^2}{2} \right] + \frac{a^2}{4} \right\} \frac{d^2 \sigma_z^{(1)}}{dz^2}.\end{aligned}\quad (10)$$

It can be seen that all stresses in the adhesive and adherents have been expressed in terms of $\sigma_z^{(1)}$. Additionally, it should be noted that the equilibrium equations for the adhesive layer cannot be fulfilled in exact sense, because of the assumption that $\sigma_z^{(A)} = 0$.

2.3 Compatibility equations

From elementary elasticity, the potential energy for component (i) is

$$\xi_p^{(i)} = \pi \int_0^L \int_r \left[\sigma_z^{(i)} \varepsilon_z^{(i)} + \sigma_{\theta}^{(i)} \varepsilon_{\theta}^{(i)} + \sigma_r^{(i)} \varepsilon_r^{(i)} + \tau_{rz}^{(i)} \gamma_{rz}^{(i)} \right] r dr dz. \quad (11)$$

Hence, the potential energies for the inner adherent (rod) $\xi_p^{(1)}$, adhesive $\xi_p^{(A)}$, and the outer adherent (timber) $\xi_p^{(2)}$ are

$$\begin{aligned}\xi_p^{(1)} &= \pi \int_0^L \int_0^a \left[\frac{\sigma_z^{(1)2}}{E^{(1)}} + 2 \left(1 - \nu^{(1)} \right) \frac{\sigma_{\theta}^{(1)2}}{E^{(1)}} \right. \\ &\quad \left. - 4 \nu^{(1)} \frac{\sigma_z^{(1)} \sigma_{\theta}^{(1)}}{E^{(1)}} + 2 \left(1 + \nu^{(1)} \right) \frac{\tau_{rz}^{(1)2}}{E^{(1)}} \right] r dr dz,\end{aligned}\quad (12)$$

$$\xi_p^{(A)} = \pi \int_0^L \int_a^b \left[2 \left(1 - \nu^{(A)} \right) \frac{\sigma_{\theta}^{(A)2}}{E^{(A)}} + 2 \left(1 + \nu^{(A)} \right) \frac{\tau_{rz}^{(A)2}}{E^{(A)}} \right] r dr dz \quad (13)$$

and

$$\begin{aligned}\xi_p^{(2)} &= \pi \int_0^L \int_b^c \left[\frac{\sigma_z^{(2)2}}{E_1^{(2)}} + \frac{\sigma_{\theta}^{(2)2}}{E_2^{(2)}} \left(1 - \nu_2^{(2)} \right) \right. \\ &\quad \left. - \frac{3 \nu_1^{(2)}}{E_1^{(2)}} \sigma_z^{(2)} \sigma_{\theta}^{(2)} + \frac{\tau_{rz}^{(2)2}}{G^{(2)}} \right] r dr dz\end{aligned}\quad (14)$$

respectively, and the compatibility equations in an integral sense can be fulfilled by minimising the potential energy

$$\begin{aligned}\xi_p &= \pi \int_0^L \left[A \sigma_z^{(1)2} + B \sigma_z^{(1)} \frac{d^2 \sigma_z^{(1)}}{dz^2} + C \left(\frac{d\sigma_z^{(1)}}{dz} \right)^2 \right. \\ &\quad \left. + D \sigma_z^{(1)} + E \left(\frac{d^2 \sigma_z^{(1)}}{dz^2} \right)^2 + F \frac{d^2 \sigma_z^{(1)}}{dz^2} + K \right] dz\end{aligned}\quad (15)$$

with respect to $\sigma_z^{(1)}$.

In Eq. (15), A, B, C, D, E, F and K are constants related to geometry and mechanical properties of the adhesive and adherents that are given in the “Appendix”.

Using the variational method, the potential energy is minimum when $\sigma_z^{(1)}$ is the solution of the differential equation [19]

$$E \frac{d^4 \sigma_z^{(1)}}{dz^4} + (B - C) \frac{d^2 \sigma_z^{(1)}}{dz^2} + A \sigma_z^{(1)} + \frac{D}{2} = 0. \quad (16)$$

$\sigma_z^{(1)}$ is obtained by solving differential Eq. (16) as

$$\sigma_z^{(1)} = -\frac{1}{2} \frac{D}{A} + C_1 e^{-w_1 z} + C_2 e^{w_1 z} + C_3 e^{-w_2 z} + C_4 e^{w_2 z}, \quad (17)$$

where the material and geometry related constants w_1 and w_2 are defined as

$$w_{1,2} = \frac{\sqrt{2}}{2E} \sqrt{-E \left(B - C \mp \sqrt{(B - C)^2 - 4AE} \right)}, \quad (18)$$

and where A, B, C, D, E, F and K are constants determined with respect to a pull–pull test setup and are given in the Appendix.

The constants $C = C_1, \dots, C_4$ in Eq. (17) can be calculated by applying the boundary conditions

$$\begin{aligned} \sigma_z^{(2)}(z=0) &= q, \quad \sigma_z^{(2)}(z=L) = 0, \\ \tau_{rz}^{(1)}(r, z=0) &= 0, \quad \tau_{rz}^{(1)}(r, z=L) = 0, \end{aligned} \quad (19)$$

and solving simultaneously the set of four equations presented in matrix form

$$\mathbf{C}_i = \begin{bmatrix} 1 & 1 & 1 & 1 \\ e^{-w_1 L} & e^{w_1 L} & e^{-w_2 L} & e^{w_2 L} \\ -w_1 & w_1 & -w_2 & w_2 \\ -w_1 e^{-w_1 L} & w_1 e^{w_1 L} & -w_2 e^{-w_2 L} & w_2 e^{w_2 L} \end{bmatrix}^{-1} \begin{Bmatrix} \frac{D}{2A} \\ f + \frac{D}{2A} \\ 0 \\ 0 \end{Bmatrix}. \quad (20)$$

The formulation for a pull–push test setup can be derived by following the same procedure as a pull–pull setup described above. By applying the loading and boundary conditions (Fig. 1b),

$$\begin{aligned} \sigma_z^{(2)}(z=0) &= 0, \quad \sigma_z^{(2)}(z=L) = q, \\ \tau_{rz}^{(1)}(r, z=0) &= 0, \quad \tau_{rz}^{(1)}(r, z=L) = 0 \end{aligned} \quad (21)$$

for the pull–push setup, and the constants A, B, C, D, E, F and K are so determined and given in the “Appendix”.

Furthermore, the normal stress component $\sigma_z^{(2)}$ in the outer adherent is obtained from the global equilibrium of the specimen as

$$\sigma_z^{(2)} = -\frac{a^2}{(c^2 - b^2)} \sigma_z^{(1)}. \quad (22)$$

2.4 Strain field

Knowing the stress field in the adhesive and adherents, the strain field can be obtained from the adopted constitutive laws for these materials.

For the outer (timber) adherent in which z is the material axis of isotropy is, the strain vector is obtained from

$$\begin{Bmatrix} \varepsilon_r^{(2)} \\ \varepsilon_z^{(2)} \\ \varepsilon_\theta^{(2)} \\ \gamma_{rz}^{(2)} \end{Bmatrix} = \begin{bmatrix} 1/E_2 & -\nu_{12}/E_1 & -\nu_{13}/E_2 & 0 \\ -\nu_{12}/E_1 & 1/E_1 & -\nu_{12}/E_1 & 0 \\ -\nu_{13}/E_2 & -\nu_{12}/E_1 & 1/E_2 & 0 \\ 0 & 0 & 0 & 1/G \end{bmatrix} \begin{Bmatrix} \sigma_r^{(2)} \\ \sigma_z^{(2)} \\ \sigma_\theta^{(2)} \\ \tau_{rz}^{(2)} \end{Bmatrix}. \quad (23)$$

Similarly, for the inner (rod) adherent which is an isotropic material,

$$\begin{Bmatrix} \varepsilon_r^{(1)} \\ \varepsilon_z^{(1)} \\ \varepsilon_\theta^{(1)} \\ \gamma_{rz}^{(1)} \end{Bmatrix} = \begin{bmatrix} 1/E & -\nu/E & -\nu/E & 0 \\ -\nu/E & 1/E & -\nu/E & 0 \\ -\nu/E & -\nu/E & 1/E & 0 \\ 0 & 0 & 0 & 2(1+\nu)/E \end{bmatrix} \begin{Bmatrix} \sigma_r^{(1)} \\ \sigma_z^{(1)} \\ \sigma_\theta^{(1)} \\ \tau_{rz}^{(1)} \end{Bmatrix}. \quad (24)$$

2.5 Stress field in Cartesian coordinate system

The stress field in the Cartesian coordinate system can be derived from the axisymmetric cylindrical stress field by the f transformation

$$\begin{bmatrix} \sigma_1 & \sigma_{12} & \sigma_{13} \\ \sigma_{21} & \sigma_2 & \sigma_{23} \\ \sigma_{13} & \sigma_{23} & \sigma_3 \end{bmatrix} = \begin{bmatrix} \sigma_\theta & 0 & \sigma_{rz} \cos \theta \\ 0 & \sigma_\theta & \sigma_{rz} \sin \theta \\ \sigma_{rz} \cos \theta & \sigma_{rz} \sin \theta & \sigma_z \end{bmatrix}. \quad (25)$$

It should be noted that the transformation in Eq. (25) has been obtained with respect to the axisymmetric nature of the GiR problem, i.e. $\sigma_{r\theta} = \sigma_{z\theta} = 0$ and the assumption that $\sigma_r = \sigma_\theta$.

2.6 Stiffness of the GiR

Integrating the $\varepsilon_z^{(1)}$ along the z axis, gives the displacement $\delta_z^{(1)}$ of the GiR joint under axial load as

$$\begin{aligned} \varepsilon_z^{(1)} &= \frac{1}{E^{(1)}} \left(\sigma_z^{(1)} - 2\nu^{(1)} \sigma_\theta^{(1)} \right) \rightarrow \\ \delta_z^{(1)} &= \frac{(D/A + \nu^{(1)} r^2)}{2E^{(1)} w_1 w_2} [C_1 w_2 (e^{-w_1 z} - 1) \\ &\quad + C_2 w_2 (1 - e^{w_1 z}) + C_3 w_1 (e^{-w_2 z} - 1) \\ &\quad + C_4 w_1 (1 - e^{w_2 z})], \end{aligned} \quad (26)$$

and the connection stiffness K_s is obtained from

$$K_s = f \pi a^2 / \delta_z^{(1)} |_{z=L, r=a}. \quad (27)$$

3 Finite element (fe) model

3.1 General

The full 3D FE models of GiR joints tested in the GIROD projects [7] are developed and analysed herein, and the results of validated FE models are used as a benchmark to demonstrate the accuracy of the analytical model. In the GIROD project, pull–pull (Fig. 2) tests were conducted on GiR joints in which 8, 12, 16 and 20 mm diameter high-strength steel rods were glued in glulam specimens made from European Spruce of class C35 [7]. In the following section, details of the FE models that can be used for analysis of GiR are discussed.

Only one half of the real specimen in the pull–pull setup was modelled due to symmetry. The outline of

the FE model is shown in Fig. 3. The diameter of the holes in the timber specimen was 2 mm larger than the diameter of the rods. The distance between the two rod ends (l_m) is $1.4l_a$ in all the specimens, where l_a is the embedment length of the rods (Fig. 2). The width of glulam ($2c$) for 8, 12, 16 and 20 mm rod were 70, 120, 120 and 140 mm respectively. The embedment length (l_a) ranges from $5d$ to $40d$, where d is the diameter of steel rod.

3.2 Timber material

Timber is an orthotropic material, but in the developed FE models the timber was modelled as a transversely isotropic material with elastic modulus parallel to the grain of $E_1 = 13000$ MPa, perpendicular to the grain of $E_2 = E_3 = E_1/30$, and shear modulus of $G_{12} = G_{13} = E_1/16$, and $G_{23} = 100$ MPa. The Timber strengths for Spruce wood of class C35 were assumed as compression and tension parallel to grain of $f_{c0} = 35.4$ MPa and $f_{t0} = 35.6$ MPa, perpendicular to the grain of $f_{c90} = 3.4$ MPa and $f_{t90} = 1.1$ MPa, respectively, shear strength of $f_v = 5.5$ MPa and rolling shear of $f_{rolling} = 1.0$ MPa.

Non-linear behaviour and failure of timber under the full 3D stress states was captured by a constitutive model developed and implemented by Gharib et al. [25]. The constitutive law used for timber is based on continuum damage mechanics (CDM), and it is able to represent both brittle and ductile failure modes of the timber elements by considering the interaction of different stress components and various failure criteria.

3.3 Steel material

The steel rods in the GiR specimens were modelled as a linear elastic–plastic hardening material. The rods in the GIROD experiments were made of Grade 8.8 steel with yield and ultimate strengths of 640 MPa and 800 MPa respectively. The strain corresponding to yield and the ultimate strength of the steel rods are 3% and 6% respectively, as reported by Steiger et al. [8].

3.4 Glue/adhesive material

The glue in the GiR specimens was assumed to be an isotropic material with brittle failure and elastic modulus of $E^{(A)} = 3000$ MPa and Poisson ratio of

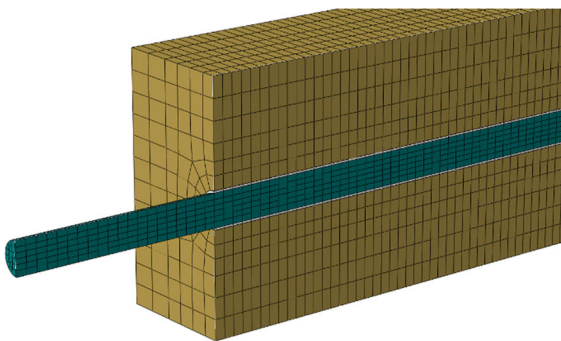


Fig. 3 Geometric outline of the GiR FE models and schematic outline of the FE mesh

$\nu^{(A)} = 0.2$. The shear strength of glue was reported higher than 18 MPa when it was used in GiR timber joints [8]. The glue thickness was 1 mm in all specimens. The thickness of glue line was relatively insignificant compared to the joint size. Accordingly, the adhesive was modelled by a traction–separation law. In this traction–separation law, linear elastic behaviour was assumed for the glue before damage initiation and a maximum nominal stress criterion in the cohesive layer was adopted for modelling the initiation of the damage. A linear softening law for normal and tangential (shear) modes was considered following the damage initiation, and the interaction between the normal mode and the shear modes (mixed mode) was considered by a power law for fracture energies of the two modes. Since the shear strength of the glue was higher than the shear strength of the timber, the failure of GiR specimens was associated with timber failure (on the interface and/or away from the interface) or yielding of the steel rods.

3.5 Boundary conditions, element type and mesh size

A displacement was applied on the tip of the steel rod while the specimen (timber) on the plane of symmetry was fixed along the z axis. The timber part and steel rod were meshed by C3D8R elements with a reduced integration scheme and the element type for the cohesive zone was COH3D8 from the ABAQUS [26] library of elements. The mesh size varied within different parts of the model and the average mesh size was set to $d/3$ (d being diameter of the steel rod). The outline of the FE mesh is shown in Fig. 3.

4 Results

4.1 Linear FE model versus analytical model

The accuracy of the closed-form analytical model described is evaluated in this example. The pull-out behaviour of a GiR joint with a 12 mm steel rod and an embedment length of 360 mm was studied and the results of analytical model are compared with the linear FE model (see Fig. 4). The example is based on one of the specimens in the GIROD project, having an ultimate load-carrying capacity of 72 kN. The serviceability range of behaviour for the GiR specimen is

taken as 40% of the ultimate load, i.e. $0.4 \times 72 = 28.8$ kN. Accordingly, a tensile force of 28.8 kN was applied to the rod that produces a normal stress of 254 MPa on the rod cross-section. The distribution of normal stress σ_z in the rod and the distribution of shear stress τ_{rz} and radial (tangential) stress σ_r (σ_θ) along the glue line obtained from the linear FE model, the proposed analytical model and Nemes' [18] model at a service load of 28.8 kN are shown in Figs. 4a, b and c. It is seen that the proposed closed-form solution shows an improvement with respect to Nemes' model in capturing the distribution of stresses (particularly the shear stress τ_{rz}) along the glue line. Moreover, the initial stiffness of the GiR calculated by the analytical solution and linear elastic FE models were 112.7 and 118 kN/mm, respectively which has a reasonable correlation with the initial stiffness of 138.2 kN/mm obtained from experimental results [7] as shown in Fig. 4d.

4.2 Non-linear FE model

The analytical and FE modelling of all GiR specimens from GIROD projects were carried out. In this section, the results of two GiR specimens with rod diameters of 8 and 16 mm and embedment lengths of 320 and 400 were reported. The GiR pull–pull specimens from the GIROD project [7] were modelled in ABAQUS software, and non-linearity of the timber, steel rod and adhesive were considered in the FE models. The distribution of normal stress σ_z in the rod and shear stress τ_{rz} on the surface of the rod (in the GLT/timber), at the service load equal to 40% of the ultimate load capacity are shown in Fig. 5. In addition, the experimental load versus displacement curves of the GiR specimens are compared with the FE and analytical model predictions in Fig. 6, which demonstrates the good correlation between the FE model predictions and experimental results. It is observable that the analytical model can adequately predict the initial stiffness of the GiR specimens with different slenderness ratios λ (the ratio of the rod embedment length to the diameter). The load versus displacement plots for specimens 12 mm rod diameters and different embedment lengths are shown in Fig. 7. The displacement in this figure is the relative displacement between the tip of the rod and a reference point on the GLT surface with a given distance from the edge of the GLT/timber. The reference points are 5, 15 and 20 mm away



Fig. 4 Distribution of **a** normal stress σ_z in the rod, **b** shear stress τ_{rz} in GLT, **c** radial stress σ_r and tangential stress σ_θ and **d** load versus displacement in GLT with 12 mm glued in rod (with embedment length of 360 mm)

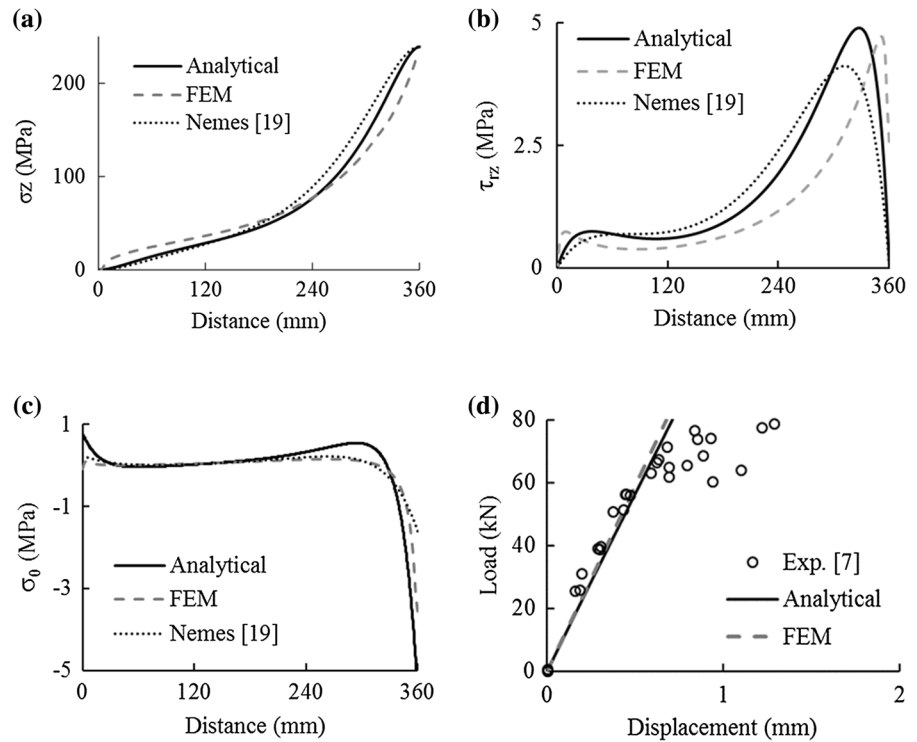
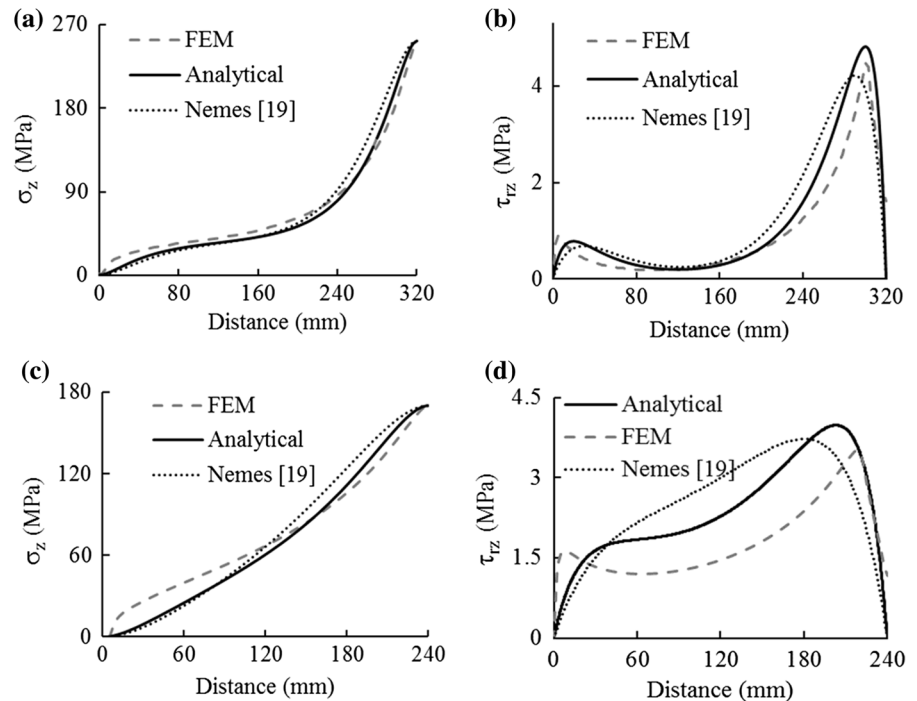


Fig. 5 **a** Normal stress σ_z in rod and **b** shear stress τ_{rz} in GLT for specimen with 8 mm rod and 320 mm embedment length, **c** normal stress σ_z in rod and **d** shear stress τ_{rz} in GLT for specimen with 16 mm rod and 400 mm embedment length, at 40% of the ultimate load



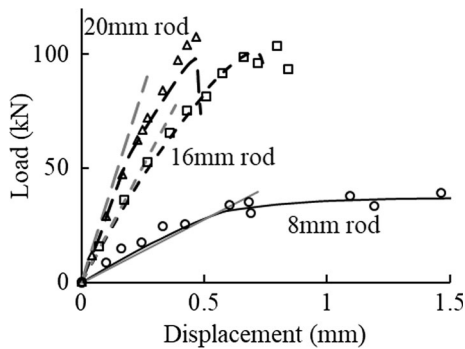


Fig. 6 Load versus displacement for 8 mm rod with embedment length of 320, 16 mm rod with embedment length of 240 and 20 mm rod with embedment length of 200 mm and the scatter data obtained from experiments [7], black curves from FE simulation and grey lines from analytical solution

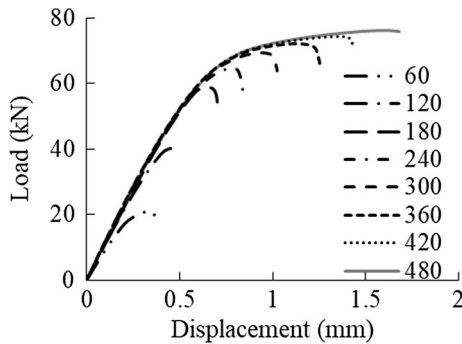


Fig. 7 Load versus displacement of GiR specimens with different embedment length and rod diameter of 12 mm

from the edge of the GLT/timber for GiR specimens with 8, 12 and 16 and 20 mm rod diameters, respectively. It is seen that the relative stiffness of the GiR is nearly constant for rod slenderness ratios λ larger than 10.

5 Parametric study and discussion

The analytical model was employed to conduct a parametric study aiming to assess the variation of the shear stress distribution along the glue line with respect to different variables.

5.1 Effect of embedment length

The embedment length has a direct impact on the shear stress distribution along the glue line. The shear stress distributions normalised with respect to maximum

shear stress (i.e. τ/τ_{\max}) for a GiR specimen with bar diameter of d and different embedment lengths ranging from $5d$ to $50d$ were evaluated. As shown in Fig. 8a, for the $5d$ embedment length, the maximum shear stress occurs in the middle of the adhesive line and the location of the maximum shear stress moves towards the far end of the adhesive line (away from the tip of the rod where the load applied) as the embedment length increases.

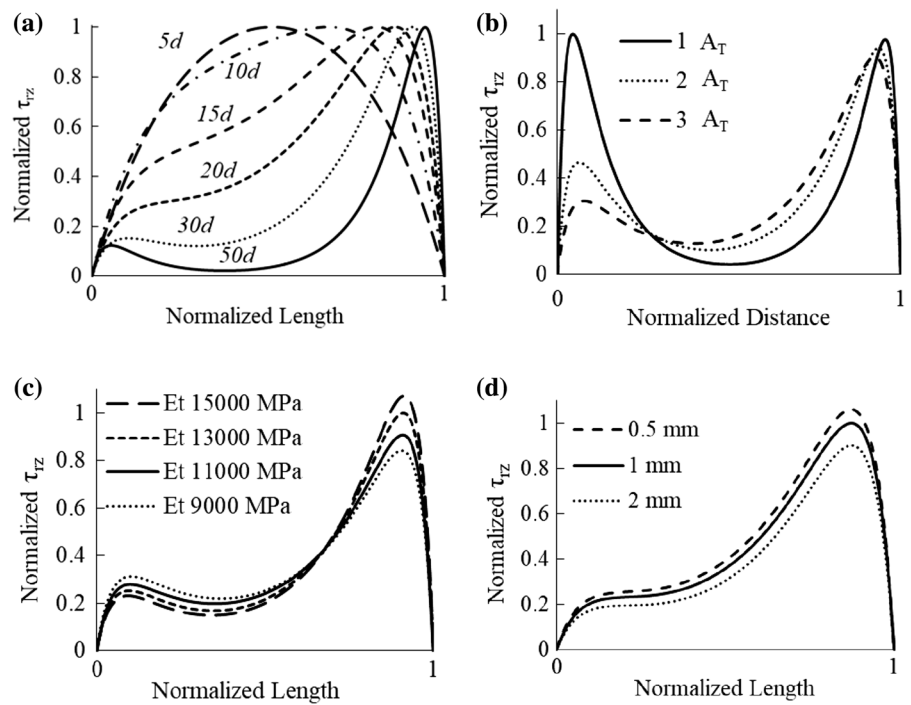
5.2 Effect of outer adherent (timber) cross-sectional area

The shear stress distributions normalised with respect to maximum shear stress (τ/τ_{\max}) for a GiR specimen with a constant bar diameter and different cross-sectional areas A_T for the timber were evaluated. It is seen that the shear stress distribution changes with respect to the area of the timber cross-section, but increasing the area of the timber cross-section from A_T to $3A_T$ only slightly reduces the maximum shear stress along the glue line (see Fig. 8b). The optimal area of timber in GiR joints can be determine using $A_T = (E_S/E_T + 1)A_R$, where E_S and E_T are elastic moduli of the steel and timber, and A_R and A_T the cross-sectional area of the rod and timber, respectively. When $A_T = (E_S/E_T + 1)A_R$, the maximum shear stress values at both ends of the rod are equal. It can be shown that by increasing the cross sectional area of timber A_T , the contribution of the third term, i.e. $C_3 w_2 e^{-w_2 z}$, in shear stress function decrease due to the decrease in C_3 and w_2 values.

5.3 Effect of material properties

The timber element in GiR joints may be made from various wood types/species with different mechanical properties. For instance, the elastic modulus of softwood and hardwood timber in the parallel to the grain direction ranges from 9000 to 15,000 MPa. Decreasing elastic modulus from 13,000 to 11,000 MPa and then to 9000 MPa results in 9.23 and 15.9% decrease in maximum shear stress, respectively. While increasing the elastic modulus to 15,000 MPa leads to 7% increase in maximum shear stress on timber part. A 27% increase in the magnitude of the maximum shear stress in the glue line is observed (see Fig. 8c) by increasing the timber elastic modulus from 9000 MPa to 15,000 MPa. In this

Fig. 8 Normalised shear stress τ_{rz} along glue line (z axis) for GiR specimen with constant rod diameter of d and varying **a** embedment length, **b** GLT cross-section area, **c** timber elastic modulus and **d** adhesive thickness



example, the elastic modulus of the timber in the perpendicular to the grain direction E_2 and shear modulus G were taken as $E_2 = E_1/30$ and $G = E_1/16$, respectively.

5.4 Effect of adhesive thickness

The adhesive thickness is usually small compared to the size of the rod and timber. The normalised shear stress τ/τ_{\max} distribution along the glue line for the GiR joints with 0.5, 1.0 and 2 mm adhesive thicknesses were evaluated and the results are shown in Fig. 8d. It was seen that increasing the thickness of the adhesive layer from 0.5 mm to 2.0 mm has reduced the maximum shear stress in the adhesive layer by 18%.

5.5 Effect of test setup (pull-pull vs pull-push)

The results of laboratory experiments have shown that the test setup (i.e. pull-pull and pull-push) can influence the load carrying capacity and stiffness of the GiR joints. The effect of the test setup in the analytical model is reflected in the boundary conditions applied. The normalised stress distributions and stiffness of a GiR joint tested in pull-pull and pull-

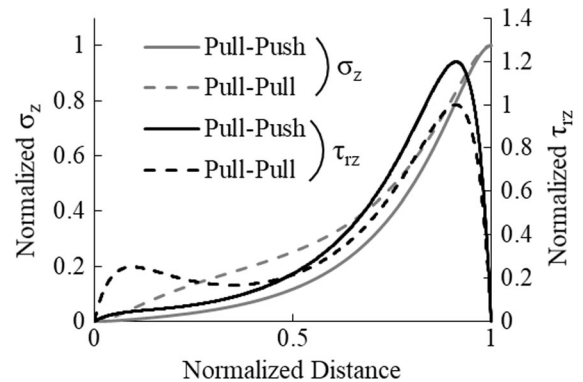


Fig. 9 Comparison of pull-pull and pull-push test setup, normalised normal stress σ_z in rod, and normalised shear stress τ_{rz} along glue line

push are shown in Fig. 9, which shows that the test setup has a minor influence on the distribution and maximum value of the normal stress σ_z (Fig. 9). However, the maximum shear stress τ_{rz} in the glue line (GLT-rod interface) in the pull-push test is around 20% higher than that of the pull-pull setup (Fig. 9). The maximum radial (tangential) stress σ_r (σ_θ) in pull-push test is also around 20% higher than the pull-pull test. Comparisons between different experimental results available in the literature have shown that the

peak strength of the GiR joints in pull–push tests is around 10–20% less than identical specimens tested in pull–pull configurations. The lower strength of the GiR joints in the pull–push experiments compared to that of pull–pull tests can be attributed to this higher maximum shear and radial (tangential) stresses predicted by the analytical model (Fig. 9). Moreover, the initial stiffness of the GiR joints in pull–push experiments is around 50% higher than the stiffness of identical GiR specimens in pull–pull tests. It should be emphasised this conclusion has been drawn with reference to geometries of specimens and mechanical properties of materials given in GIROD project.

6 Discussion of failure modes

Four distinctive failure modes have been identified for the GiR joints and the onset and location of these failure modes is strongly dependent on the material properties and geometry of the rod and timber [5]. The results of laboratory experiments in the literature (in particular the GIROD project) and non-linear FE simulations carried out in this study were employed to elucidate these failure modes.

- Failure due to yielding of the rod (Mode I): yielding of rod occurs when the embedment length is sufficient to provide for transmission of the axial force from the rod to the timber through shear. The yielding of rod is a ductile failure mode and the most desirable failure mode for GiR joints. The average value of shear stress along the glue line obtained from $\tau_{rz} = P/\pi dL$ versus the slenderness

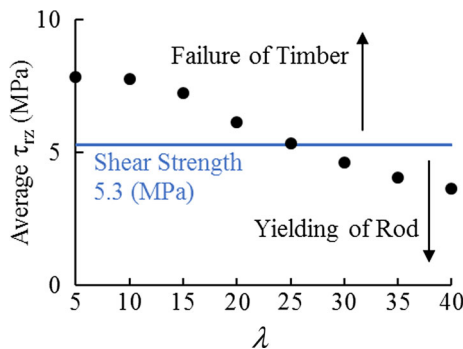


Fig. 10 Average shear stress in the GLT versus slenderness λ = embedment length/diameter and governing failure mode of the specimens

ratio λ of the rod is plotted in Fig. 10. Assuming an average shear strength of 5.3 MPa for timber as per the GIROD project data, it is observed that for GiR joints with a slenderness ratio λ larger than 25, the dominant failure mode is associated with yielding of steel and for $\lambda < 25$ the dominant failure mode is associated with failure of the timber (Fig. 10). This observation is consistent with the failure modes reported in GIROD project and valid for specimens with material properties and geometries similar to that of GIROD project.

- Failure due to tension parallel to grain (Mode II): this failure mode occurs when the normal tensile stress in the timber exceeds the tensile strength parallel to the grain (also parallel to the loading direction). This failure mode is brittle and therefore should be prevented in design of GiR joints. Assuming that parallel to the grain stresses are independent of the other stress components and adopting Saint–Venant’s principle, the onset of this failure mode can be related to the area of timber A_T and rod A_R , tensile strength f_{t0} of timber and yield strength f_y of the rod. This failure mode may be prevented if $F/A_T < f_y$, $A_R/A_T < f_{t0}$, and accordingly maximum area of the rod in the GiR joints should be limited to $A_R \leq A_T f_{t0}/f_y$. However, the stress concentration at the end of the rod may cause tensile stresses higher than the average calculated stress (i.e. F/A_T). Hence, the simple method proposed should be used as a tool for preliminary check to safeguard GiR joints against tensile failure of the timber.
- Failure due to interaction of tension perpendicular to grain and shear stresses (Mode III): according to the criterion proposed by Sandhaas [27] and implemented in ABAQUS by Gharib et al. [25],

$$\left(\frac{\sigma_\theta}{f_{t90}}\right)^2 + \left(\frac{\sigma_{rz} \cos \theta}{f_v}\right)^2 > 1 \text{ and } \left(\frac{\sigma_\theta}{f_{t90}}\right)^2 + \left(\frac{\sigma_{rz} \sin \theta}{f_v}\right)^2 > 1 \quad (28)$$

where f_{t90} is tensile strength perpendicular to the grain and f_v is the shear strength of the timber. It should be noted this failure mode comprises of timber splitting and/or timber failure in shear. If the tangential/radial stresses dominate the structural behaviour, then the failure of GiR joint is predominantly associated with splitting in the

timber, otherwise the higher shear stresses may cause shear failure in the timber. According to Tlustochowicz et al. [5], a small edge distance (less than $2.5d$) may cause splitting of the timber. Both splitting and shear failure in timber are brittle failure modes, and should be prevented in the design of GiR joints.

- Brittle failure of adhesive layer governed by the interaction between tensile and shear stresses (Mode IV);

$$\left(\frac{\sigma_{\theta}^A}{f_t^A}\right)^2 + \left(\frac{\sigma_{rz}^A \cos \theta}{f_v^A}\right)^2 > 1, \quad (29)$$

where f_t^A and f_v^A are the tensile and shear strengths of the adhesive.

7 Conclusions

This paper has investigated the behaviour of glued-in-rod (GiR) joints under short-term axial loading. An analytical model for GiR joints was developed by solving the governing differential equations for a system comprising of the rod, adhesive and timber. Proper boundary conditions for the pull–pull and pull–push test setup were applied and closed-form formulas for stress field and stiffness of the GiR joint are derived. Moreover, linear and non-linear finite element (FE) analyses of GiR joints from GIROD project [7] were carried out. The validated FE models were used as a benchmark to demonstrate the accuracy of the closed-form analytical model and also conduct a parametric study in which effects of different parameters on the behaviour of GiR joints are highlighted. The following conclusions are drawn from the results of analytical and FE modelling.

- Within the linear elastic range of the response, the analytical solution developed can efficiently predict the stress field in the rod, adhesive and timber with a reasonable accuracy that is comparable with the FE simulations.
- Comparing the results of pull–pull and pull–push setups obtained from the analytical model shows that the radial (tangential) and shear stresses in the adhesive layer (or rod–timber interface) in the pull–push case is around 20% higher than that of a pull–pull setup. The lower strength of GiR joints in

a pull–push setup compared to a pull–pull configuration (observed in the laboratory experiments) can be attributed to this higher tangential and shear stresses which are predicted by the analytical model.

- The results of the analytical model show that the initial stiffness of the GiR joints in pull–push experiments is around 50% higher than the initial stiffness of identical GiR specimens in a pull–pull loading scenario.
- Physical modelling of the thin adhesive layer in non-linear continuum-based FE analysis of GiR joints can be prohibitive. However, the results of non-linear 3D continuum-based FE modelling in this study showed that behaviour and failure of the adhesive layer can be adequately captured by traction–separation laws without physically modelling the adhesive layer.
- Using simple failure criteria in conjunction with stress fields predicted by the analytical model can represent the initiation and evolution of the damage along the glue line in the rod–timber interface.

Acknowledgements The work in this paper was funded by a Discovery Project (DP160104092) awarded to the second and third authors by the Australian Research Council. This support is acknowledged with thanks.

Compliance with ethical standards

Conflicts of interest The authors declare that they have no conflict of interest.

Appendix

The constants for the analytical solution of the pull–pull test setup are

$$A = \frac{1}{2} \frac{a^2}{E^{(1)}} - \frac{1}{2} \frac{a^4}{E_1^{(2)}(b^2 - c^2)}$$

$$B = -\frac{a^4 v^{(1)}}{4E^{(1)}} - \frac{3}{16} \frac{a^4 v_{12}^{(2)}[b^4 - c^4 + 4b^2 c^2 \ln(c/b)]}{E_2^{(2)}(b^2 - c^2)^2}$$



$$C = \frac{1}{8} \frac{(1 + \nu^{(1)})a^4}{E^{(1)}} - \frac{1}{24} \frac{a^2(a^4 - b^4)(1 + \nu^{(A)})}{b^2 E^{(A)}} - \frac{1}{16} \frac{a^4[4c^4 \ln(b/c) + b^4 - 4b^2c^2 + 3c^4]}{G^{(2)}(b^2 - c^2)^2}$$

$$D = \frac{a^4 f}{E_1^{(2)}(b^2 - c^2)}$$

$$A = \frac{1}{2} \frac{a^2}{E^{(1)}} - \frac{1}{2} \frac{a^4}{E_1^{(2)}(b^2 - c^2)}$$

$$B = -\frac{a^4 \nu^{(1)}}{4E^{(1)}} - \frac{3}{16} \frac{a^4 \nu_{12}^{(2)}[b^4 - c^4 + 4b^2c^2 \ln(c/b)]}{E_2^{(2)}(b^2 - c^2)^2}$$

$$E = \frac{1}{48} \frac{(1 - \nu^{(1)})a^6}{E^{(1)}} + \frac{a^4(1 - \nu^{(A)})}{E^{(A)}(a - b)(b^2 - c^2)^2}$$

$$\left[\left[-\frac{1}{8}(a + b)(a^2 + b^2) \left(c^2 \ln\left(\frac{c}{b}\right) + b^2 - c^2 \right)^2 \right] + \left[\frac{1}{6}(a^2 + ab + b^2) \left(c^2 \ln\left(\frac{c}{b}\right) + b^2 - c^2 \right) \left(2ac^2 \ln\left(\frac{c}{b}\right) + (a + b)(b^2 - c^2) \right) \right] + \left[-\frac{1}{16}(a + b) \left(2ac^2 \ln\left(\frac{c}{b}\right) + (a + b)(b^2 - c^2) \right)^2 \right] \right]$$

$$+ \frac{1}{192} \frac{a^4(1 - \nu_{13}^{(2)})}{E_2^{(2)}(b^2 - c^2)^2} \left[12b^4c^2 \ln\left(\frac{b}{c}\right) - 24b^2c^4 \ln\left(\frac{c}{b}\right)^2 - 2b^6 + 3b^4c^2 - 6b^2c^4 + 5c^6 \right]$$

$$F = \frac{3}{16} \frac{fa^4 \nu_{12}^{(2)}(b^4 - c^4 + 4b^2c^2 \ln(c/b))}{E_2^{(2)}(b^2 - c^2)^2}$$

$$K = -\frac{a^4 f^2}{2E_1^{(2)}(b^2 - c^2)}$$

$$C = \frac{1}{8} \frac{(1 + \nu^{(1)})a^4}{E^{(1)}} - \frac{1}{24} \frac{a^2(a^4 - b^4)(1 + \nu^{(A)})}{b^2 E^{(A)}} - \frac{1}{16} \frac{a^4[4c^4 \ln(b/c) + b^4 - 4b^2c^2 + 3c^4]}{G^{(2)}(b^2 - c^2)^2}$$

$$D = 0$$

The constants for the analytical solution of the pull–push setup are



$$E = \frac{1}{48} \frac{(1 - \nu^{(1)})a^6}{E^{(1)}} + \frac{a^4(1 - \nu^{(A)})}{E^{(A)}(a-b)(b^2 - c^2)^2} \left[\left[-\frac{1}{8}(a+b)(a^2 + b^2) \left(c^2 \ln\left(\frac{c}{b}\right) + b^2 - c^2 \right)^2 \right] + \left[\frac{1}{6}(a^2 + ab + b^2) \left(c^2 \ln\left(\frac{c}{b}\right) + b^2 - c^2 \right) \left(2ac^2 \ln\left(\frac{c}{b}\right) + (a+b)(b^2 - c^2) \right) \right] + \left[-\frac{1}{16}(a+b) \left(2ac^2 \ln\left(\frac{c}{b}\right) + (a+b)(b^2 - c^2) \right)^2 \right] \right] + \frac{1}{192} \frac{a^4(1 - \nu_{13}^{(2)})}{E_2^{(2)}(b^2 - c^2)^2} \left[12b^4c^2 \ln\left(\frac{b}{c}\right) - 24b^2c^4 \ln\left(\frac{c}{b}\right)^2 - 2b^6 + 3b^4c^2 - 6b^2c^4 + 5c^6 \right]$$

$$F = 0$$

$$K = 0$$

References

- Yang S, Wu Z, Hu X, Zheng J (2008) Theoretical analysis on pullout of anchor from anchor-mortar-concrete anchorage system. *Eng Fract Mech* 75(5):961–985
- Vallée T, Bletz-Mühldorfer O, Myslickt S, Grunwald C, Walther F, Baton L (2016) Glued-in rods in hardwood and hardwood laminated veneer lumber-report on a large experimental campaign. In: WCTE 2016—world conference on timber engineering
- Fragiacomo M, Batchelar M (2012) Timber frame moment joints with glued-in-steel rods I: design. *ASCE J Struct Eng* 138(6):789–801
- Parida G, Johnsson H, Fragiaco M (2013) Provisions for ductile behavior of timber-to-steel connections with multiple glued-in rods. *J Struct Eng (U S)* 139(9):1468–1477. [https://doi.org/10.1061/\(ASCE\)ST.1943-541X.0000735](https://doi.org/10.1061/(ASCE)ST.1943-541X.0000735)
- Thustochowicz G, Serrano E, Steiger R (2011) State-of-the-art review on timber connections with glued-in steel rods. *Mater Struct/Materiaux et Constructions* 44(5):997–1020. <https://doi.org/10.1617/s11527-010-9682-9>
- Steiger R, Serrano E, Stepinac M, Rajčić V, O'Neill C, McPolin D, Widmann R (2015) Strengthening of timber structures with glued-in rods. *Constr Build Mater* 97:90–105. <https://doi.org/10.1016/j.conbuildmat.2015.03.097>
- Aicher S, Holz F (2001) Characteristic axial resistance of threaded rods glued-in spruce dependant on adhesive type a complementary database for the GIROD project. Universität Stuttgart, Otto-Graf-Institut
- Steiger R, Gehri E, Widmann R (2007) Pull-out strength of axially loaded steel rods bonded in glulam parallel to the grain. *Mater Struct/Materiaux et Constructions* 40(1):69–78. <https://doi.org/10.1617/s11527-006-9111-2>
- Widmann R, Steiger R, Gehri E (2007) Pull-out strength of axially loaded steel rods bonded in glulam perpendicular to the grain. *Mater Struct/Materiaux et Constructions* 40(8):827–838. <https://doi.org/10.1617/s11527-006-9214-9>
- Otero Chans D, Cimadevila JE, Gutiérrez EM (2008) Glued joints in hardwood timber. *Int J Adhes Adhes* 28(8):457–463. <https://doi.org/10.1016/j.ijadhadh.2008.04.008>
- Otero Chans D, Estévez Cimadevila J, Martín Gutiérrez E (2013) Withdrawal strength of threaded steel rods glued with epoxy in wood. *Int J Adhes Adhes* 44:115–121. <https://doi.org/10.1016/j.ijadhadh.2013.02.008>
- Serrano E (2001) Glued-in rods for timber structures—a 3D model and finite element parameter studies. *Int J Adhes Adhes* 21(2):115–127
- Madhoushi M, Ansell MP (2017) Effect of glue-line thickness on pull-out behavior of glued-in GFRP rods in LVL: finite element analysis. *Polym Testing* 62:196–202. <https://doi.org/10.1016/j.polymertesting.2017.06.029>
- Del Senno M, Piazza M, Tomasi R (2004) Axial glued-in steel timber joints-experimental and numerical analysis. *Holz als Roh-und Werkstoff* 62(2):137–146. <https://doi.org/10.1007/s00107-003-0450-1>
- Xu BH, Bouchair A, Racher P (2012) Analytical study and finite element modelling of timber connections with glued-in rods in bending. *Constr Build Mater* 34:337–345. <https://doi.org/10.1016/j.conbuildmat.2012.02.087>
- Lubkin L, Reissner E (1956) Stress distribution and design data for adhesive lap joints between circular tubes. *Trans ASME J Appl Mech* 78:1213–1221
- Shi YP, Cheng S (1993) Analysis of adhesive-bonded cylindrical lap joints subjected to axial load. *J Eng Mech* 119(3):584–602. [https://doi.org/10.1061/\(ASCE\)0733-9399\(1993\)](https://doi.org/10.1061/(ASCE)0733-9399(1993))

18. Nemeş O, Lachaud F, Mojtabi A (2006) Contribution to the study of cylindrical adhesive joining. *Int J Adhes Adhes* 26(6):474–480. <https://doi.org/10.1016/j.ijadhadh.2005.07.009>
19. Nemes O, Lachaud F (2009) Modeling of cylindrical adhesively bonded joints. *J Adhes Sci Technol* 23(10–11):1383–1393. <https://doi.org/10.1163/156856109X432983>
20. Upadhyaya P, Kumar S (2015) Pull-out capacity of adhesive anchors: an analytical solution. *Int J Adhes Adhes* 60:54–62. <https://doi.org/10.1016/j.ijadhadh.2015.03.006>
21. Kumar S, Scanlan JP (2010) Stress analysis of shaft-tube bonded joints using a variational method. *J Adhes* 86(4):369–394. <https://doi.org/10.1080/00218461003704329>
22. Kumar S, Khan MA (2016) An elastic solution for adhesive stresses in multi-material cylindrical joints. *Int J Adhes Adhes* 64:142–152. <https://doi.org/10.1016/j.ijadhadh.2015.10.009>
23. Kumar S, Khan MA (2016) A shear-lag model for functionally graded adhesive anchors. *Int J Adhes Adhes* 68:317–325. <https://doi.org/10.1016/j.ijadhadh.2016.04.010>
24. Prieto-Muñoz PA, Yin HM, Testa RB (2014) Mechanics of an adhesive anchor system subjected to a pullout load. I: Elastic analysis. *J Struct Eng (United States)* 140(2):13052. [https://doi.org/10.1061/\(asce\)st.1943-541x.0000826](https://doi.org/10.1061/(asce)st.1943-541x.0000826)
25. Gharib M, Hassanieh A, Valipour H, Bradford MA (2017) Three-dimensional constitutive modelling of arbitrarily orientated timber based on continuum damage mechanics. *Finite Elem Anal Des* 135:79–90. <https://doi.org/10.1016/j.finel.2017.07.008>
26. ABAQUS, User's Manual, Version 6.9, Dassault Systèmes (2009)
27. Sandhaas C (2012) Mechanical behaviour of timber joints with slotted-in steel plates. Delft University of Technology, Netherlands